Formation and growth of complex precipitates in 316L austenitic steel during long-term annealing experiments

Michael Klimenkov · Michael Rieth ·
Anton Möslang

Abstract Transmission electron microscopy as well as corresponding analytical techniques, such as energy dispersive X-ray analysis, electron energy loss spectroscopy, and elemental mapping via Gatan imaging filter, have been used to study the growth sequence of complex precipitates with a TiN core formed in a commercial 316L(N) austenitic steel after creep experiments at 600 °C. It was found that the TiN precipitates, which originally exist in the as-delivered steel, serve as nucleation sites for intermetallic and Cr-containing carbide precipitates. The evolution of precipitate formation and growth was analyzed based on undeformed sample screw heads after 84, 164, 5,481, 41,000, and 85,000 h annealing.

Introduction

The austenitic stainless steels play an important role in the modern world. They are probably the most important class of corrosion-resistant metallic materials. Among many applications the austenitic steel 17/12-2—CrNiMo steel 316L(N) (DIN 1.4909) is used or envisaged for conventional and nuclear power plant construction as well as in the International Nuclear Fusion Project. A number of experimental investigations worldwide have already been carried out to determine the material properties of this steel type in the conventional stress and temperature range. The presented creep studies were focused on three batches in the temperature range of 500–750 °C for periods of up to 85,000 h. The final experimental results, which show the creep rupture strength and creep tests, were published in [1, 2]. The developed and experimentally proven creep models were published in [2, 3].

The long-term high temperature exposure of the steel leads to the precipitation of carbide, nitride, or intermetallic phases. The process changes the nominal composition of the steel that contains substantial amount of alloying elements and consequently worsens the mechanical and corrosion properties. The summaries of the sizable experimental and theoretical works published during last three–four decades were published in several reviews [4–6]. The time-temperature-precipitate and compositional diagrams presented in the reviews include comprehensive information about growth of solitary precipitates, their location, and expected influence on the mechanical properties. However, in addition to solitary precipitates, the formation of complex precipitates was detected in austenitic steels [7, 8]. Such precipitates typically have a Ti or Nb carbo-nitride core and (Fe, Cr, Mo) carbide or intermetallic shell around. Apart from few exceptions [7, 8], the published studies report only the existence and composition of complex precipitates omitting their formation process [9]. Here the potential of new transmission electron microscopy (TEM) methods, for studying detailed elemental composition of precipitates, was shown for a specific case. As can be estimated, based on evaluation of TEM images obtained from the sample aged at 600 °C for 85,000 h, approximately 10–20% of precipitates inside the grains have a TiN core. Thus, the presence of such precipitates and their influence on decomposition process of austenitic steels cannot be neglected. The aim of the present article is to show their formation and growth process on annealing stages ranging from 0 to 85,000 h.

M. Klimenkov (✉) · M. Rieth · A. Möslang
Institute for Materials Research I, Forschungszentrum Karlsruhe GmbH, Hermann-von-Helmholtz-Platz 1, 76344 Eggenstein-Leopoldshafen, Germany
e-mail: michael.klimenkov@imf.fzk.de

Various analytical TEM methods have been applied to study complex precipitates after long-term creep and creep rupture experiments on austenitic 316L steel. TEM combined with modern analytical techniques like Energy Dispersive X-rays (EDX) analysis, Electron Energy Loss Spectroscopy (EELS), and Energy Filtered TEM (EFTEM) were used for detailed characterization of complex precipitates. These powerful methods for detecting precipitates and determination of spatial elemental distribution were widely used in the past [10, 11]. The EDX and EELS methods, which generally supply similar information, have natural sensitivity limitations [12]. The application of both methods enables the comprehensive characterization of the chemical composition of precipitates with spatial resolution of about 1 nm.

Experimental

The presented investigations have been performed on 316L(N) steel with heat no. 11477 from Creusot-Marell (CRM). This heat had been delivered as 40-mm hot-rolled plate with a final heat treatment at 1,100 °C followed by water quenching. Quality assurance reported this batch as nearly free of δ-ferrite (<1%). The chemical composition of this steel is given in Table 1.

The samples after 84, 164, 5,481, 41,000, and 85,000 h creep test at 600 °C have been chosen for the TEM characterization. The untreated material in the "as-delivered" state has also been chosen for investigations. Specimens were cut from the undeformed screw heads and mechanically thinned to the thickness of $\sim$130 μm. From these discs, TEM samples of 3 mm diameter were punched and electro-polished in a TENUPOL device using H_2SO_4 + 80% CH_3OH as electrolyte. The samples were additionally cleaned for a few minutes with an Ar ion beam at a low angle in a Precise Ion Polishing System made by Gatan Ltd.

The investigations were performed using a FEI Tecnai 20 F microscope equipped with a Gatan Image Filter for EFTEM and EELS measurements as well as with a high-angle annular dark field (HAADF) detector for the scanning TEM. The microscope was operated at 200 kV accelerating voltage with a field emission gun. In order to optimise the signal-to-noise ratio in the elemental maps, the largest—150 μm (acceptance semi-angle β = 15 mrad)—condenser aperture on the microscope was used. Energy-filtered elemental maps were recorded using three window and jump

ratio methods. The EELS experiments were performed in the scanning TEM (STEM) regime using the HAADF detector with a camera length of 100 mm for particle imaging. Experimental conditions were chosen such that the collection semi-angle was 13 mrad. For EELS measurements, an energy resolution of 1.1 eV and dispersions of 0.1 eV/channel for one-edge spectra and 0.5 eV/channel for multi-edge spectra were employed.

The EDX spectra were recorded using an EDAX Si/Li detector with ultra-thin window. The quantitative EDX experiments were performed on the precipitates which were located on or near the specimen edge in order to avoid the influence of the matrix. TEM images were recorded by means of a 1024 × 1024 pixels Gatan CCD camera. The electron beam used for imaging and analysis has a probe size of 1.0–1.2 nm. Due to the broadening effect the limit of spatial analytical information has been estimated to 1.5 ± 0.2 nm.

The natural limitations of analytical methods have been taken into account for the interpretation of measured elemental maps. Due to the poor sensitivity at low energies of EDX analysis, EEL spectroscopy for detection of carbon and nitrogen was used. On the other hand, the observed Mo-M edge is characterized by a 200 eV broad maximum ranging from 250 to 450 eV. This edge profile influences the background fitting and herewith the distribution of intensity in the image. The influence of Mo-M_3 edge (392 eV onset energy) is especially strong on the N-K edge (397 eV onset energy). The effect is readily identifiable in the N and Mo EFTEM maps. This makes EDX method more suitable for Mo detection than EELS. The presence of light elements, such as carbon and nitrogen, on the one hand and metals like molybdenum on the other, in the same precipitate, require application of both analytical methods.

Results

The spatially resolved EELS and EDX analyses were used for the determination of the chemical composition of particles which were found in the "as-delivered" material (Fig. 1). A typical precipitate with 50 nm size is shown in the HAADF image (Fig. 1a). The investigation of the chemical composition of the precipitate has been performed using line scan method. The electron beam has scanned along the drawn line with simultaneous acquisition for 2 s of EDX and EELS signals in each point. The EEL spectra were recorded in the range from 230 to 730 eV that covers C-K, N-K, Ti-L, Cr-L, and Fe-L EEL edges. Figure 1b presents an EEL spectrum without background correction which was obtained from the particle center. The edges of the indicated elements can be clearly identified in the spectrum.

Table 1 The composition of 316L(N) steel Fe-bal., wt.%

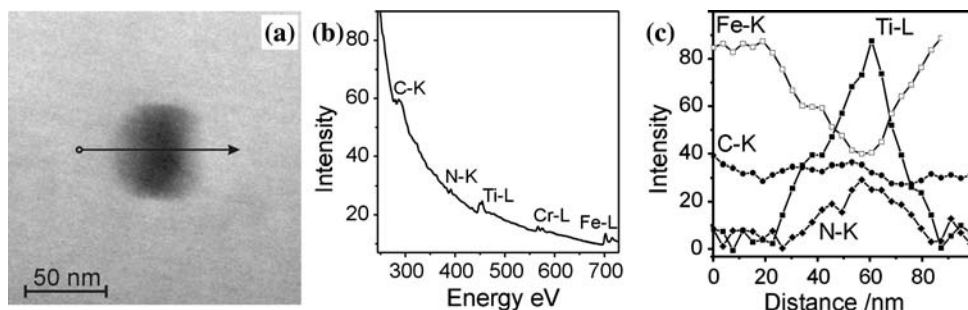| Ti	C	Mn	Cr	Ni	Mo	N
0.02	0.02	1.8	17.0	12.5	2.4	0.06

Fig. 1 HAADF image of the TiN inclusion with a marked line for the scanning experiment (**a**), an example of the EEL spectrum acquired from the middle of the particle, which demonstrates its composition (**b**), and relative intensity of marked C-K, N-K, and Ti-L EELS edges as well as Fe-Kα EDX signal along the scanning line (**c**)

The spatial distribution profiles of Fe, Ti, N, and C elements are plotted in Fig. 1c. The intensity of Y-axis has been normalized to arbitrary units for EDX and EELS methods separately. The profiles of light elements such as C, N, and Ti were imaged with EELS. Fe distribution was drawn using Fe-Kα EDX signal which shows a better signal-to-noise ratio than the Fe-L EEL signal. The intensity of EEL edges was calculated after background correction separately for each edge using inverse power law: $A*E^{-r}$, where E represents the energy (eV) and A and r are interpolation parameters. The statistical error in the element distribution profiles was estimated by variation of line intensities in the homogenous area to the value of 3–5%. Ti-L and N-K EELS signals show maxima at the center of precipitate whereas the C-K EELS signal remains constant through the whole scanning line. The none-zero intensity of C-K edge indicates contamination of the sample surface with amorphous carbon due to intensive electron

irradiation, while the constant value shows its absence inside the precipitate. The decreased Fe concentration on the precipitate is inversely proportional to the increased Ti and N concentration (Fig. 1c). The intensity of Fe signals reduces on the particle center only to the value of about 45%. Such behavior shows that the investigated TiN precipitate is embedded in the matrix and not located on its surface. The profiles of Cr, Ni, and Mo, which were not plotted, show the same concentration characteristics as Fe.

Spatially resolved chemical analysis of TiN particles on the initial tempering stages was performed using EDX mapping. Figure 2a shows a HAADF image of a TiN precipitate in the "as-delivered" steel. The EDX maps of Ti, Fe, Cr, Ni, and Mo elements in the imaged area are represented in Fig. 2b–f. The bright contrast on the Ti map (Fig. 2b) confirms that the imaged precipitate consists of TiN. Darker contrast of the Fe, Cr, Ni, and Mo maps indicates decreasing concentration on the precipitate. The maps did not indicate

Fig. 2 EDX mapping of a TiN precipitate in the as-delivered sample. (**a**) Represents the HAADF image of the precipitate, whereas the elemental maps obtained using the Ti Kα, Fe Kα, Cr Kα, Ni Kα and Mo - Lα EDX signals are represented in (**b–f**), respectively
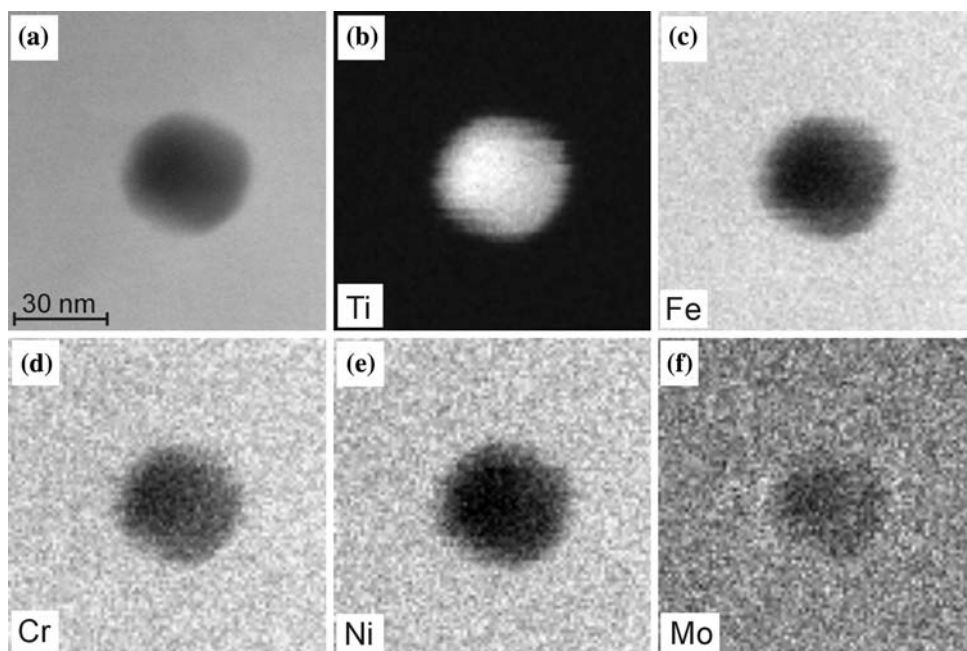
any increasing/decreasing concentration of these alloying elements in the area around the TiN precipitate. Figure 3a and c shows HAADF images of TiN precipitates in the samples after 84 and 164 h treatment, respectively. The corresponding Mo maps are depicted in the Fig. 3b and d.

After 5,481 h annealing at 600 °C, two different precipitate types inside grains were found which have TiN nuclei. A HAADF image of such a precipitate is presented in Fig. 4a. The precipi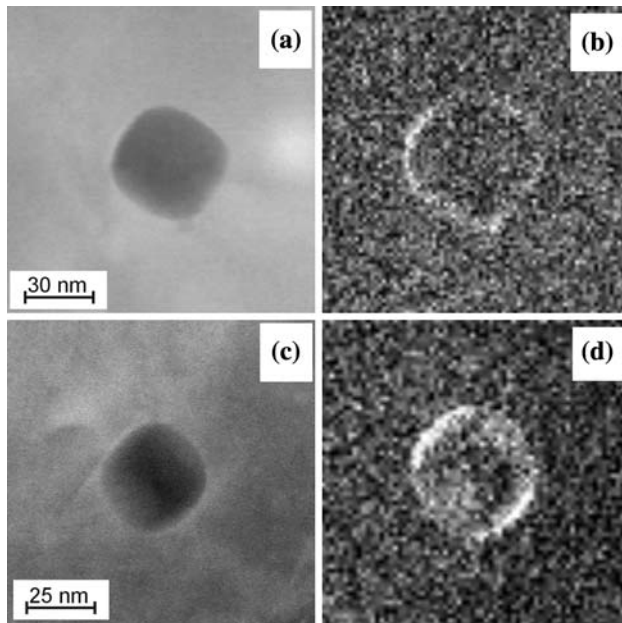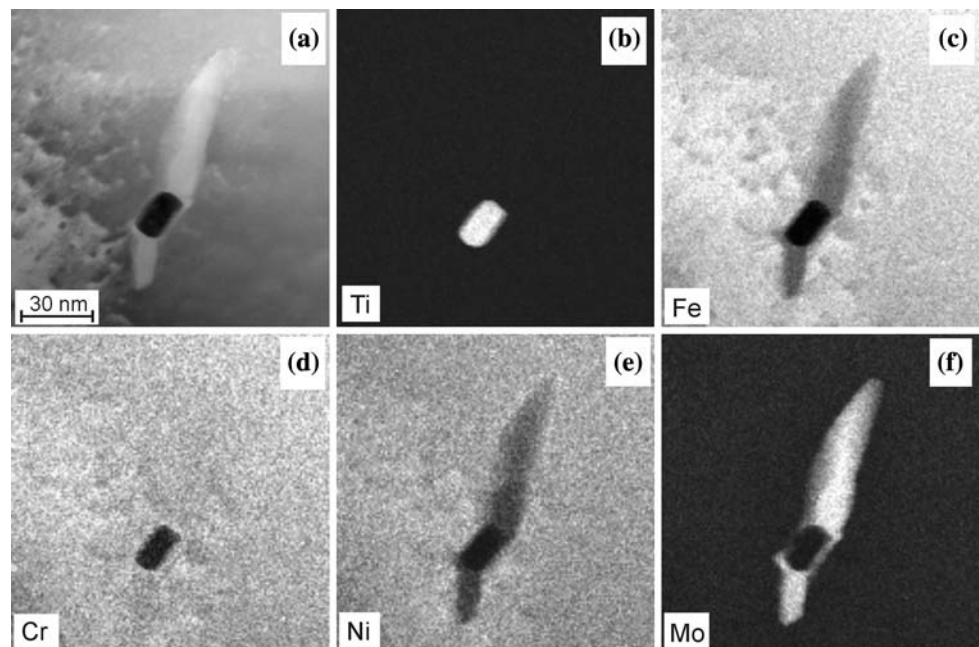tate consists of a 25 nm diameter core, which is visible with the darker contrast, and a 120 nm long and 15–25 nm broad tail, which is located on both sides of the core. The Ti map presented in the Fig. 4b confirms that the core consists of Ti-containing phase. As it was shown by numerous EELS and high-resolution TEM (HRTEM) investigations the Ti-rich precipitates are always TiN. The darker contrast in the Fe and Ni maps shows deficiency of these elements in the precipitate compared to the surrounding matrix (Fig. 4c, e). The absence of any contrast in the Cr map indicates that the Cr concentration in the grown precipitate is 17%. This is exactly the same concentration as in the matrix (Fig. 4d). The Mo concentration increases in the tail as is shown by the bright contrast in Mo map (Fig. 4f). The chemical composition of the Mo-containing tail was investigated using local EDX analysis. The quantitative evaluation of EDX spectra obtained from the tail fraction of the complex precipitate is presented in the Table 2. The error in the chemical composition is connected with uncertainty in the specimen thickness and could be estimated to 1%. The precipitates of this type will be referred as "type one" in the article.

The HAADF image of a complex precipitate with a TiN core of the second type is presented in the Fig. 5a. The shell, which completely surrounds the core, consists of two different phases. In the Ti map two TiN cores are visible (Fig. 5b). The Fe and Ni maps show the deficiency of these

Fig. 3 The HAADF images of a TiN precipitate (**a**, **c**) and Mo EDX maps of the corresponding areas around the precipitates (**b**, **d**) in the samples after 84 h and 164 h treatment, respectively

Table 2 The composition of Laves-phase tails measured by EDX method, wt.%

Fe	Mo	Cr	Ni	Si
41.0 ± 1.0	37 ± 1.0	17 ± 1.0	4 ± 0.5	1.5 ± 0.5

Fig. 4 EDX maps of a complex precipitate of the first type in the sample after 5,481 h annealing. (**a**) Represents the HAADF image of the precipitate, whereas the elemental maps obtained using the Ti-K$_\alpha$, Fe-K$_\alpha$, Cr-K$_\alpha$, Ni-K$_\alpha$, and Mo-L$_\alpha$ EDX signals are represented in (**b–f**), respectively

Fig. 5 EDX maps of a complex precipitate of the second type in the sample after 5,481 h annealing. (**a**) Represents the HAADF image of the precipitate, whereas the elemental maps obtained using the Ti-K_α, Fe-K_α, Cr-K_α, Ni-K_α, and Mo-L_α EDX signals are represented in (**b–f**), respectively
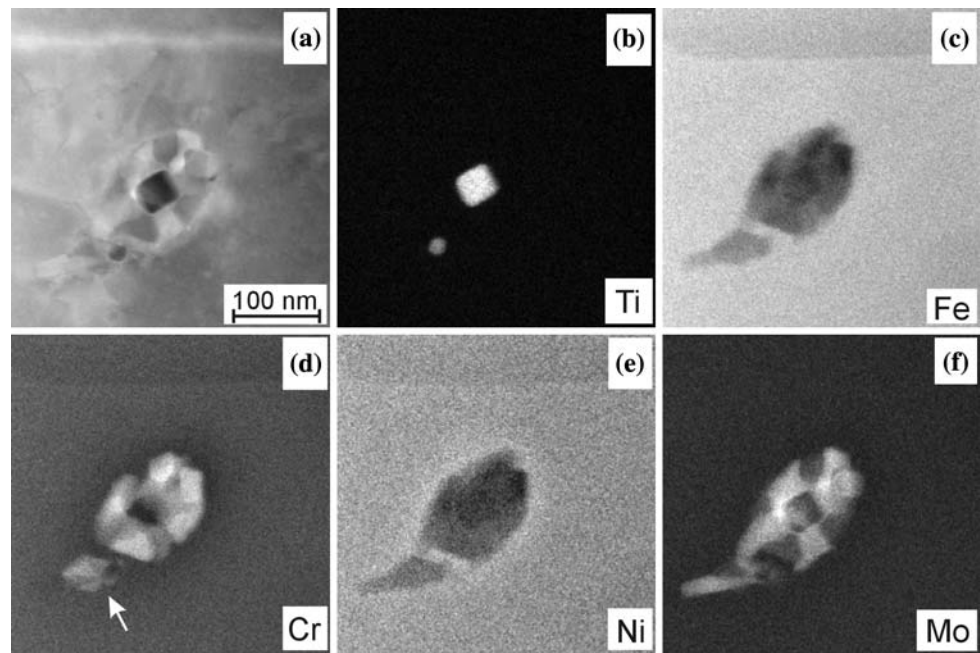
elements in the whole precipitate (Fig. 5c, e). In the Cr map two separate precipitates can be clearly distinguished (Fig. 5d): one is located exactly around the larger TiN core and the other, Cr-rich precipitate (marked with the arrow), is closely located at the smaller core. The Mo map shows the formation of a complete Mo-rich shell around the larger nucleus (Fig. 5f). The intensity of Mo and Cr signals is not homogeneously distributed in the shell. The considering shows that the spatial distribution of these elements inversely correlate to each other (Fig. 5d, f). The areas of the shell that have a brighter contrast in Mo map exhibit a darker contrast in the Cr map and vice versa.

In the spatially resolved analytical analysis of second type precipitate shown in Fig. 5, the decomposition of matrix around precipitate can also be clearly observed. The matrix area of 20 nm thickness around the precipitate exhibits the 10–15% enrichment of Ni and 10–15% depletion of Cr (Fig. 5d, e). This area is visible with slightly brighter or darker contrasts in the respective elemental maps.

Both discussed types of complex precipitates with TiN core were found in the sample after 41,000 h annealing. In Fig. 6 EFTEM investigations of the second type precipitate are presented. The EFTEM elemental mapping enables determination of spatial distribution of all main matrix elements as well as C and N. The bright-field image (Fig. 6a) presents a complex precipitate with the size of about 400 nm. It can be clearly seen that the precipitate consists of different phases. The whole precipitate is visible in the Fe map with the dark contrast (Fig. 6b). The Ti and N maps presented in Fig. 6c and d prove the existence of a TiN nucleus in the middle of the precipitate. Formation of a

Cr- and C-rich shell around the nucleus can be clearly observed in the C and Cr maps (Fig. 6e, f). The investigations using electron diffraction and HRTEM methods show that this Cr carbide phase has the $M_{23}C_6$ structure. The quantitative evaluation of a EDX spectrum results in $(Cr_{13}Fe_4Mo_6)C_6$ carbide composition (Table 3). The quantitative data have been normalized without the consideration of carbon. The quantification of light elements is possible only with considerable error. The equal spatial distribution of these elements is also a proof of a carbide shell formation during extended aging times. The carbide shell completely surrounds the nucleus, with the exception of two narrow channels, which are visible with a darker contrast in both maps (C, Cr). These channels are filled with Mo-rich intermetallic phase which is also visible in the Mo map (Fig. 6g). This is presumably Laves phase.

The elemental maps of second type precipitates in the sample tempered for 85,000 h at 600 °C is shown in Fig. 7. The HAADF image is presented in Fig. 7a. The spatial distribution of Ti shows the location of the TiN core with the size of 40 nm (Fig. 7b). The dark contrast in Fe and Ni maps shows their deficiency in the precipitate (Fig. 7c, d). The closed shell around TiN core consisting of $M_{23}C_6$ phase is visible with a bright contrast in the Cr map (Fig. 7e). The tails which consist of Laves phase grow around the $M_{23}C_6$ shell in form of a cross. These tails are clearly visible in the Mo map (Fig. 7f).

The complex precipitates of the first type were found in both samples after 41,000 h and 85,000 h annealing. The nature of the precipitates did not change on these aging stages. The EFTEM investigations of such precipitate, which has formed in the sample after 85,000 h annealing, are

Fig. 6 EFTEM investigations of the second type complex precipitate. (**a**) Represents the TEM bright-field image; (**b–g**) Represents the Fe-L$_{2,3}$, Ti-L$_{2,3}$, N-K, C-K, Cr-L$_{2,3}$, and Mo-M$_{4,5}$ elemental maps, respectively
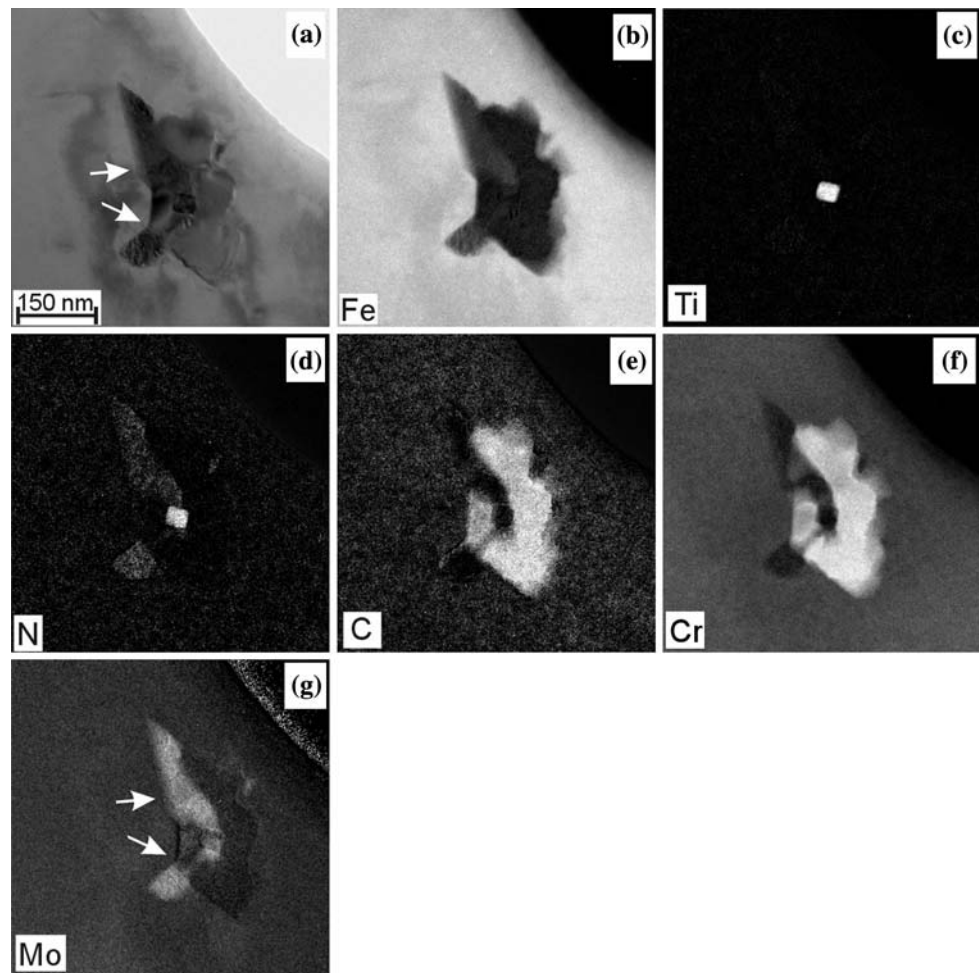

Table 3 The composition of carbide phase measured by EDX method, wt.%

Fe	Mo	Cr
16.5 ± 1.0	24.0 ± 1.0	59.5 ± 1.0

presented in the Fig. 8. The precipitate of 500 nm × 120 nm size is visible with the dark contrast in the bright-field image (Fig. 8a). The hardly visible nucleus inside the precipitate is marked with an arrow. This precipitate is located near the specimen edge and herewith surrounded by the matrix in the image plane. This produces the darker contrast in the Fe map (Fig. 8b). The increased Mo concentration is visible in the Mo map (Fig. 8c). The nucleus inside the precipitate is visible with darker contrast in these both maps (Figs. 8b, c). C map presented in the Fig. 8d shows absence of C inside the nucleus and Laves-phase precipitate. Two bright lines in the C map can be referred to the carbon contamination of the specimen surface during line scan analysis of closed-by precipitate (not imaged). The spatial distribution of Ti and N in corresponding maps (Figs. 8e, f) clearly confirms the TiN composition of the nucleus.

Usually, the length of first type precipitates increases to the value of 300–500 nm and the width to the value of 80–150 nm after 41,000 h aging. After 85,000 h aging, the length and width of precipitates grows to 400–700 nm and to 100–200 nm, respectively.

Discussion

The specimens for TEM characterization were cut from the undeformed screw heads which were exposed at the same temperature as the gauge lengths. With this step, we have tried to avoid the complex discussions concerning influences of mechanical tension on the formation of precipitates. The influence leads possibly to the changes in the precipitates morphology and distribution which can not be reliably detected using TEM. On the other hand, the influence of different annealing times on the formation of precipitates can be clear detected.

The TEM investigation of the 316L steel on the initial tempering stages, which were defined as 0–300 h, shows the presence of only one type of precipitate type inside the

Fig. 7 EDX maps of a complex precipitate of second type in the sample after 85,000 h aging. (**a**) Represents the HAADF image of the precipitate, whereas the elemental maps obtained using the Ti-K$_\alpha$, Fe-K$_\alpha$, Cr-K$_\alpha$, Ni-K$_\alpha$, and Mo-L$_\alpha$ EDX signals are presented in (**b–f**), respectively
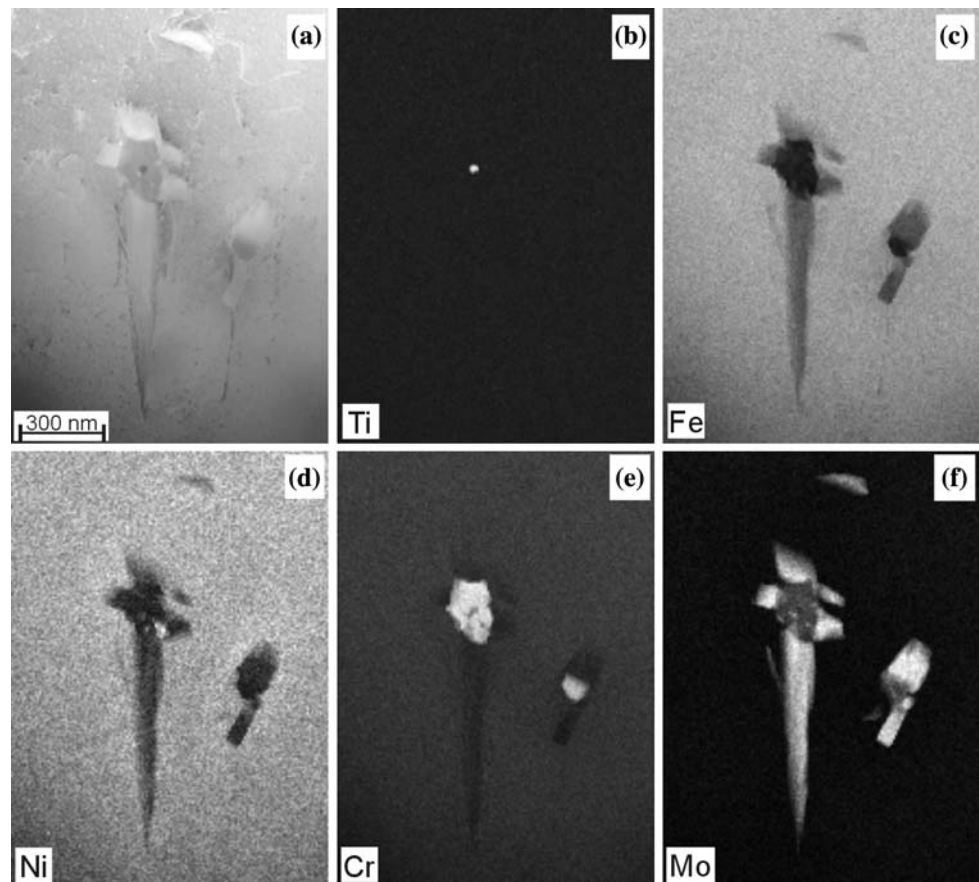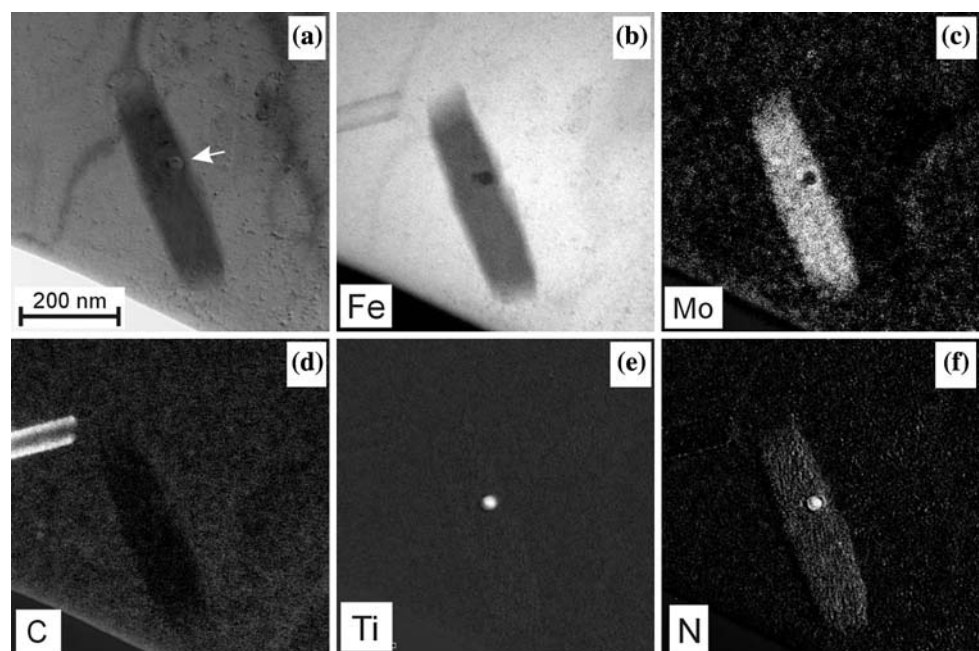

Fig. 8 EFTEM investigations of the first type complex precipitate. (**a**) Represents TEM bright-field image; (**b–f**) Represents Fe-L$_{2,3}$, Mo-M$_{4,5}$, C-K, Ti-L$_{2,3}$, and N-K elemental maps, respectively

grains—TiN. These precipitates, which mainly have cubic or cuboid form with sizes of 20–70 nm, are depicted in several HAADF images (Figs. 1a, 2a, 3a, c). As was shown in previous publications, Ti in austenitic steels can form

nitride, carbide or even carbo-nitride precipitates, which have a similar crystalline structure [13, 14]. Their chemical analysis was performed using combined application of EELS and EDX methods (Fig. 1). The spatial density of

these precipitates in the "as-delivered" material was estimated to be $(1–5) \times 10^{14}$ cm^{-3}. The thermal treatment for several hundred hours does not lead to a visible change.

As can be derived from published "time-temperature precipitation diagrams," the decomposition process in austenitic steels starts after a few hundreds hours treatment at 600 °C [4, 5]. The first small new precipitates were observed only on the grain boundaries. This is understandable as the grain boundaries serve as a nucleation sites for the different precipitates [4]. The TiN particles, which are located inside the grains, do not show any visible changes by conventional TEM. The application of EDX mapping with nanosize electron probe enables evidence of Mo-containing shell formation around the TiN precipitates (Figs. 2, 3). The maps drawn using Mo-L EDX signal clearly indicates the presence of a thin shell around TiN particle after 84 h annealing (Fig. 3b) which was not present in the "as-delivered" material (Fig. 2f). The elemental maps of Fe, Cr, and Ni presented in Fig. 2c–e did not show any enrichment of these alloying elements around TiN particle. The typical thickness of the shell after 84 h treatment was estimated to be about 2 nm (Fig. 3b). The shell thickness increases after 164 h treatment to values of about 5–10 nm (Fig. 3d). The shell has not a constant thickness around the TiN core. It grows preferentially on opposite sides of the precipitate (Fig. 3d). The growth direction correlates possibly with the [100]TiN orientation and does not show any correlation with matrix orientation. The measurement of the shell composition referring to other alloying elements appears impossible due to the small shell thickness and disturbing signal from the matrix.

The annealing during 5,481 h leads to an increasing value of spatial concentration of the complex precipitates with a TiN core to $(0.7–2) \times 10^{15}$ cm^{-3}. The value is approximately 2–3 times higher than the density of TiN particles in the steel on the initial annealing stages. The process leads apparently to the precipitation of new TiN particles inside grains which can serve as nucleation center for other phases. The complex precipitations can be separated based on their morphology in two types.

In the first precipitates type the TiN core is surrounded by a Mo-containing tail with a longer form (Fig. 4). The chemical composition of the tail (Table 2) was found to be similar to that reported for the Laves phase [5]. HRTEM investigations, published elsewhere, confirm that the tails around the TiN core with increased Mo-concentration consist of Laves phase [15]. The comparison of this result with a time–temperature precipitation diagram shows that formation of Laves phase inside grains at 600 °C was observed only after 10^4 h aging [4, 5]. This means that we observe formation of Laves phase at a markedly earlier annealing time. However, the results should not be considered as a disagreement but as a complement to the

ones already published. As we suppose, presence of TiN nucleus inside grains plays a crucial role in the formation process of Laves phase on earlier stages. Because of the low density of TiN precipitates they can be considered rather as exceptions. This type of precipitate can be considered as the Laves phase, which has continuously grown around the core.

In the complex precipitates of the second type, the shell around the TiN core consists of two phases: the Mo-rich Laves phase and Cr-rich $M_{23}C_6$ phase. The spatial resolved analytical EDX study of such precipitation is presented in Fig. 5. In the Ti map it is visible that this precipitate has two TiN cores with approximately 80 nm distance between them. Such a close appearance of two TiN particles is rather unusual. However, their average density increases approximately by a factor of 2–3 after 5,481 h aging. The smaller particles form obviously during tempering. The $M_{23}C_6$ and Laves phase are superimposed in the shell. It can be suggested that $M_{23}C_6$ phase forms around the precipitate on the later annealing stages, when the Laves-phase shell already existed. The $M_{23}C_6$ phase did neither form a third shell nor form separate but closely located part, as would be expected. It replaces the Laves phase in the regions around the TiN core. This replacement process leads to the formation of the shells with such a complex structure.

The appearance of complex precipitates of the second type correlates with precipitation of $M_{23}C_6$ phase according to the published time–temperature diagrams [4, 5]. Grain boundaries serve as the preferred sites for the precipitation of $M_{23}C_6$ phase after aging for several thousands hours. The already-formed TiN particles with a Mo-containing shell serve also as the nucleation sites for $M_{23}C_6$ precipitation during these annealing stages.

The presence of complex precipitates of two types with TiN core was also observed at later annealing stages, which cover the aging procedure of 41,000 h and 85,000 h. The density of precipitates with TiN nucleus in both samples was estimated to be $(3–8) \times 10^{15}$ cm^{-3}. That means, an increase by a factor of 3 approximately corresponds to a sample which has been aged for 5,481 h. This increase indicates that TiN particles precipitate statistically in the matrix continuously during the annealing time. These particles serve immediately as the nuclei for further precipitation.

The annealing causes further coarsening of both types of complex precipitates. The precipitates of the first type increase their length to several hundred nanometers and the width to 100–150 nm. From comparing, e.g., the size of precipitates after 5,481, 41,000, and 85,000 h, can be supposed the monotonic growth of such precipitates during the whole annealing time. The form of the first type of precipitates (Fig. 8) is similar to the solitary Laves-phase

precipitates which can also be found inside the grains after 41,000 and 85,000 h. This is understandable because precipitation of Laves phase in austenitic steels was reported after $(5-10) \times 10^3$ h [4, 5]. However, the size of solitary precipitates do not exceed 500 nm, their formation took place at later stages than complex precipitates of the first type. The analysis presented in the Fig. 8 clearly shows that precipitates of the both types have the nuclei of the same TiN composition.

The TEM analysis of the second type of precipitates shows obvious changes of their size and morphology. The chemical composition of the precipitate was studied using EDX elemental mapping and EFTEM (Figs. 6, 7). The investigations show that the Mo-rich Laves phase is displaced from the area directly around TiN nucleus and forms tail-like precipitates in the outer regions of the $M_{23}C_6$ shell. From the elemental maps, it is clear that $M_{23}C_6$ phase surrounds the TiN nucleus with the exception of two narrow channels, which are marked with arrows in TEM image (Fig. 6a) and in Mo map (Fig. 6e). These channels are filled with Mo-rich Laves phase (Fig. 6g). The EXD maps of a precipitate after 85,000 h aging show that $M_{23}C_6$ phase build a closed shell around the TiN nucleus (Fig. 7e). The displacement process of the Laves phase to the outer shell in the presented precipitates is completed in most precipitates at this annealing stage. The precipitates of second type can occasionally be found with a morphology, where Laves-phase tails have a small contact area with the TiN core. Thus, precipitates are possibly formed on later annealing stages so that this process is not completed yet.

The composition of the precipitates was determined using both EELS and EDX methods. EELS measurement confirms the presence of carbon inside the shell and denies its presence inside the Mo-rich tails. The Laves-phase tails usually have a length of several hundred nanometers; occasionally their size can exceed 1 μm (Fig. 7).

Conclusion

In the present work, the formation process of complex precipitates with a TiN was investigated. The results of the study are clearly described by a time-dependence growth sequence (Fig. 9). On the earlier aging stages, which cover several hundred hours, a thin Mo-rich shell forms around the TiN core. Annealing for a few thousand hours results in the formation of two different types of complex precipitates which grow in different ways. The complex precipitates of the first type consist of a TiN core surrounded by only Mo-rich Laves phase. Tails of Laves
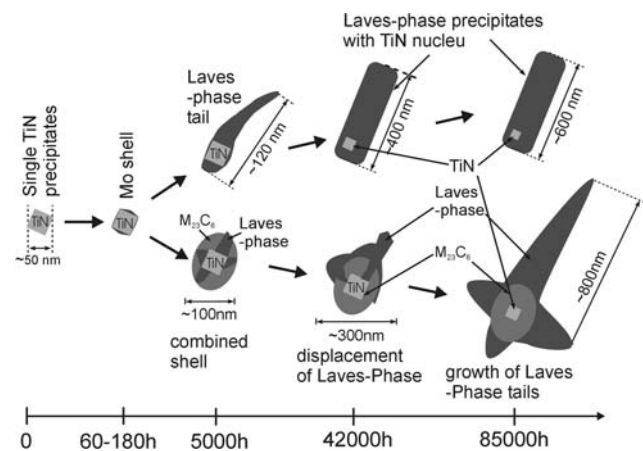

Fig. 9 Schematic growth sequence of complex precipitates with a TiN core at different annealing stages

phase grow to a length of 800 nm after 85,000 h annealing as shown in the upper sequence in the diagram. Growth of precipitates of the second type, which additionally have a Cr-rich $M_{23}C_6$ shell, is presented on the lower sequence. This carbide phase displaces continuously the Mo-rich Laves phase from TiN core to the outer regions. The knowledge of the growth sequence of complex precipitates will contribute to a detailed understanding of the decomposition process in austenitic steels and, consequently, to the understanding of steel properties and degrading during thermo-mechanical treatment.

References

1. Schirra M (1999) Nucl Eng Des 188:381
2. Rieth M, Falkenstein A, Graf P, Heger S, Jäntsch U, Klimiankou M, Materna-Morris E, Zimmermann H (2004) Creep of the austenitic steel AISI 316 L(N). Experiments and models. Scientific Report; FZKA-7065
3. Rieth M (2007) J Nucl Mater 367:915
4. Padilha AF, Rios P-R (2002) ISIJ Int 42:325
5. Sourmail T (2001) Mater Sci Technol 17:1
6. NRIM-Creep Data Sheet No. 42-1996; National Research Institute for Metals, Tokyo, Japan (1996)
7. Sasmal B (1997) J Mater Sci 32:5439
8. Craven AJ, He K, Carvie LAJ, Baker TN (2000) Acta Mater 48:3857
9. Thomas PJ, Midgley PA (2001) Ultramicroscopy 88:179
10. Warbichler P, Hofer F, Hofer P, Letofsky E (1998) Micron 29:63
11. Hattestrand M, Nilsson JO, Stiller K, Liu P, Andersson M (2004) Acta Mater 52:1023
12. Reimer L (1997) Transmission electron microscopy. Springer series in optical science, vol 36, p 430
13. Chen Z, Loretto MH, Cochrane RC (1987) Mater Sci Technol 3:836
14. Scott CP, Chaleix D, Barges P, Rebischung V (2002) Scripta Mater 47:845
15. Padilha AF, Escriba DM, Materna-Morris E, Rieth M, Klimenkov M (2007) J Nucl Mater 362:132